OPTICS

Enhancing monolayer photoluminescence on optical micro/nanofibers for low-threshold lasing

Feng Liao[1]*, Jiaxin Yu[1]*, Zhaoqi Gu[1]*, Zongyin Yang[2], Tawfique Hasan[2], Shuangyi Linghu[1], Jian Peng[1], Wei Fang[3], Songlin Zhuang[1], Min Gu[4], Fuxing Gu[1]†

Although monolayer transition metal dichalcogenides (TMDs) have direct bandgaps, the low room-temperature photoluminescence quantum yields (QYs), especially under high pump intensity, limit their practical applications. Here, we use a simple photoactivation method to enhance the room-temperature QYs of monolayer MoS_2 grown on to silica micro/nanofibers by more than two orders of magnitude in a wide pump dynamic range. The high-density oxygen dangling bonds released from the tapered micro/nanofiber surface are the key to this strong enhancement of QYs. As the pump intensity increases from 10^{-1} to 10^4 W cm^{-2}, our photoactivated monolayer MoS_2 exhibits QYs from ~30 to 1% while maintaining high environmental stability, allowing direct lasing with greatly reduced thresholds down to 5 W cm^{-2}. Our strategy can be extended to other TMDs and offers a solution to the most challenging problem toward the realization of efficient and stable light emitters at room temperature based on these atomically thin materials.

INTRODUCTION

Because of the direct bandgaps in the visible and near-infrared regions, monolayer transition metal dichalcogenides (TMDs) have opened notable opportunities for the development of integrated light-emitting devices (*1*–*3*). Their atomically thin nature enhances the Coulomb interaction between electrons and holes and can support stable excitons at room temperature, which dominate the photoluminescence (PL) emissions in monolayer TMDs. However, the defects introduced during the fabrication and processing steps provide substantial nonradiative recombination pathways. In addition, as the pump intensity increases, the generated high-density carriers in this atomic thickness enhance many-body interactions such as nonradiative exciton-exciton annihilation (*4*). These factors lead to low PL emission intensity of monolayer TMDs and PL quantum yields (QYs) strongly dependent on the pump intensity. Taking monolayer MoS_2 as an example, the reported PL QYs are in the range of 0.01 to 0.6% in typical samples prepared by mechanical exfoliation and chemical vapor deposition (CVD) (*5*). In practical light-emitting applications, improving PL QYs of monolayer TMDs under high pump intensity conditions is extremely important (*6*). For example, for sensing and imaging devices, using sufficient emission intensity generated by high-power excitation can reduce the signal acquisition time of the detectors and enable real-time monitoring of the samples. In particular, for optical amplifiers and lasers that must operate at high pump intensity to achieve population inversion, the low PL QYs make it difficult to provide sufficient optical gain from these atomically thin monolayers. This forces us to use only high-quality factor optical microcavities to achieve lasing actions (*7*–*11*). These microcavities require complex microfabrication and transfer manipulation processes that may degrade the PL QYs of monolayer TMDs due to the surface contamination and cracks (*12*).

Since the PL QYs of monolayer TMDs strongly depend on the pump intensity, it is highly desirable to study the PL emissions over a wide pump dynamic range so that we can determine whether a certain method for enhancing PL emissions of monolayer TMDs is suitable for practical device applications. To date, many efforts such as molecular adsorption (*13*, *14*), defect engineering (*15*, *16*), and strain modulation (*17*) have been exploited to improve the PL emissions of monolayer TMDs. However, most of these studies have been carried out under certain constant pump intensity. Superacid treatment has been reported to enhance the QYs of transferred monolayer MoS_2 and WS_2 in wide pump dynamic range, reaching nearly 100% at low excitation levels (<10^{-2} W cm^{-2}) (*5*, *18*). Nevertheless, as the pump intensity increases, the QYs of these samples are gradually reduced and fail to provide sufficient optical gain. In addition, this method is only effective for sulfur-based monolayer TMDs, and the environmental stability of treated samples is not satisfactory. Therefore, achieving high and stable PL QYs of monolayer TMDs over a wide pump dynamic range, especially under high pump intensity conditions, is still one of the main challenges that need to be overcome to enable their efficient light-emitting applications.

Amorphous silica is a key material in the field of optoelectronics, fiber-optic communications, and optical microcavities and is also commonly used as a substrate for growing and supporting two-dimensional materials. Previous work has shown that the density of trap states on silica surfaces (*19*, *20*) is in the range of ~10^{10} to 10^{14} cm^{-2}, which is comparable to the carrier concentrations in chemically pristine monolayer TMDs (*5*, *13*). As material size decreases to the micro/nanoscale, the surface-to-volume ratios and the numbers of free dangling bonds increase, making the chemical reactivity of micro/nanomaterials different from their bulk counterparts. This suggests that silica-based micro/nanomaterials with enhanced chemical reactivity may be used as substrates not only to grow TMDs but also to modulate their optoelectronic properties due to the presence of additional dangling bonds at the surface. Silica micro/nanofibers (MNFs), physically drawn from standard optical fibers, have remarkable features such as low propagation loss, high fractional evanescent fields, and tailorable waveguide dispersion and

[1]Laboratory of Integrated Opto-Mechanics and Electronics, Shanghai Key Laboratory of Modern Optical System, Engineering Research Center of Optical Instrument and System (Ministry of Education), University of Shanghai for Science and Technology, Shanghai 200093, China. [2]Cambridge Graphene Centre, University of Cambridge, Cambridge CB3 0FA, UK. [3]State Key Laboratory of Modern Optical Instrumentation, College of Optical Science and Engineering, Zhejiang University, Hangzhou 310027, China. [4]Laboratory of Artificial Intelligence Nanophotonics, School of Science, RMIT University, Melbourne, Victoria 3001, Australia.
*These authors contributed equally to this work.
†Corresponding author. Email: gufuxing@usst.edu.cn

offer a promising building block or platform for both fundamental research and device applications (*21*, *22*).

In this work, we first grow single-crystal monolayer MoS_2 on tapered silica MNFs. We then use a simple photoactivation strategy to obtain strongly enhanced and highly stable PL QYs in a wide pump dynamic range at room temperature. The taper-drawing process greatly lowers the activation energy from siloxane bonds in bulky amorphous silica to free oxygen dangling bonds on the tapered MNFs; the high-density oxygen dangling bonds released by photoactivation is the key to achieving strong PL enhancement. Compared with the planar monolayer samples grown on silica substrates, as-photoactivated MoS_2 monolayers on MNFs exhibit more than two orders of magnitude PL enhancement, with QYs ranging from ~30 to 1% as pump intensity increases from 10^{-1} to 10^4 W cm^{-2}. These enhanced QY values are about 6 to 20 times higher than those by chemical treatment as the pump intensity increases from 10 to 10^3 W cm^{-2} (*23*). The high QY allows direct realization of room-temperature continuous-wave (CW) lasing with greatly reduced thresholds down to 5 W cm^{-2}. Our strategy offers an effective solution to the challenging problem of achieving high PL QYs at room temperature, making it practical to realizing monolayer-based coherent light sources.

RESULTS

In amorphous silica materials such as standard optical fibers, silicon and oxygen atoms (≡Si—O—Si≡) bridge with each other in random ring structures, with the majority of six-membered rings (*24*, *25*). By drawing a CO_2 laser–heated standard single-mode optical fiber (outer diameter, 125 μm), a tapered MNF with a diameter comparable to the scale of light wavelength (~1 μm) can be fabricated, as shown in Fig. 1A and inset (see Materials and Methods and section S1). This large size deformation will cause the high-membered rings to cleave into low-membered rings, the majority of which will be three-membered rings. Because of the decreased siloxane bond angles, these low-membered rings are highly strained, raising the average internal energy of these bonds (*26*). Since the taper-drawing process greatly lowers the activation energy from siloxane bonds (≡Si—O—Si≡) in conventional bulky amorphous silica, under high-intensity light irradiation (e.g., a 532-nm CW laser used in our work), these highly strained siloxane bonds can be easily excited to release high-density oxygen dangling bonds (≡Si—O·, oxygen half-filled 2p orbital) on the MNF surface.

Figure 1B shows the PL spectra from different MNFs and a planar substrate under activation intensity of 2.1×10^5 W cm^{-2} (see Materials and Methods and section S2). A broad band centered around 1.86 eV is observed in the microfiber with a diameter (D_{fiber}) of 3.1 μm, which agrees with the reported PL position of oxygen dangling bonds (*25*). This band is weak in the microfiber with D_{fiber} = 10.2 μm, and no obvious band is observed around this position in the planar substrate. Figure 1C shows that the PL intensity of 1.86-eV band in the microfiber (D_{fiber} = 3.1 μm) increases as the excitation intensity increases. The strained three-membered rings are considered as the precursor of oxygen dangling bonds, and its Raman mode at 606 cm^{-1} can be used for evaluating the amount of oxygen dangling bonds. As shown in Fig. 1D, the intensity of the 606 cm^{-1} Raman peak increases as the MNF diameter decreases. We further characterize the structural reconstruction on the MNF surfaces using a high-resolution atomic force microscope (AFM) in Fig. 1E. As the diameter of originally drawn MNF decreases, the surface roughness increases, which is induced by the mechanically tapering process that directly breaks the Si—O bonds and generates more dangling bonds. Furthermore, when irradiated with high-intensity light, the surface roughness of those two microfibers increases, and the thinner one (D_{fiber} = 3.2 μm) increases much more. These results demonstrate the generation and existence of oxygen dangling bonds on MNF surface in the tapering and high-intensity light irradiation process.

By directly breaking Si—O bonds in six-membered rings to generate oxygen dangling bonds, the energy needed is as high as ~9 eV, which is equivalent to the bandgap value of silica. Our calculation shows that the energy of generating an oxygen dangling bond from a three-membered ring is in the range of ~4.0 to 8.0 eV, as denoted in Fig. 1A. The tapering process greatly increases the surface energy of MNFs, which allows using a 532-nm CW laser via multiphoton absorption to achieve oxygen dangling bonds on the surface. As illustrated in Fig. 1C, when in contact with monolayer semiconductors such as n-type MoS_2, these reactive oxygen dangling atoms can fill the sulfur vacancies (absorbing ~0.45 electrons per dangling oxygen atom; see section S3) or bridge with neighboring sulfur atoms (absorbing ~0.41 electrons per dangling oxygen atom) in monolayer MoS_2, forming stable localized sites through the electron transfer from MoS_2 (*20*, *27*). These two processes will reduce the nonradiative exciton-exciton annihilation and strongly enhance the PL emissions of monolayer MoS_2.

Figure 2A presents a schematic of monolayer MoS_2 grown on silica MNFs with a uniform diameter and prolate microbottle structures. During the CVD growth process (see Materials and Methods and section S4), a single-crystal triangular domain first nucleates on the MNF surface randomly and then laterally extends its size along the cylindrical surface of the MNF. Figure 2B shows a typical optical image and its corresponding PL image of a small triangular MoS_2 layer on a microfiber with D_{fiber} = 6.1 μm. The AFM image in Fig. 2C confirms its monolayer nature with a thickness of ~0.8 to 1.0 nm. As the growth time increases, a micro/nanotube structure is formed in the azimuthal direction of the MNF, which then extends its size only along the axial direction of the MNF. Figure 2D shows a typical microtube structure with D_{fiber} = 5.5 μm. The clean and uniform surface and two sharp boundary edges with an angle of approximately 60° are seen (section S5), indicating its single-crystal nature. The single-crystal monolayers can be fabricated on MNFs with diameters down to several hundred nanometers (section S6), and as-grown monolayers can have lengths of single domains up to 100 μm. Figure 2E shows a single-crystal monolayer microtube structure grown on a microfiber (D_{fiber} = 5.4 μm) with a domain length of ~77 μm. From the corresponding PL image, it is observed that some emission at the microfiber surface is transformed into a guided mode along the microfiber and is emitted at the distal end. Monolayer MoS_2 can also be grown on the microbottle structures, with typical results shown in section S7.

Figure 2F presents the Raman spectra of monolayer MoS_2 grown on a planar silica substrate and several different fibers with diameters decreasing from 125 μm to 470 nm. It is observed that as the size of MNF decreases, the out-of-plane vibrational mode A_{1g} maintains its position at ~402.6 cm^{-1}; while the strain-sensitive in-plane vibrational mode E^1_{2g} exhibits a red shift from 386.2 to 380.5 cm^{-1}, but no obvious splitting of the E^1_{2g} mode occurs (*28*). We also observe similar red shifts in the spectra of the PL emissions (Fig. 2G) and the absorption (section S8) of as-grown monolayer MoS_2 on MNFs.

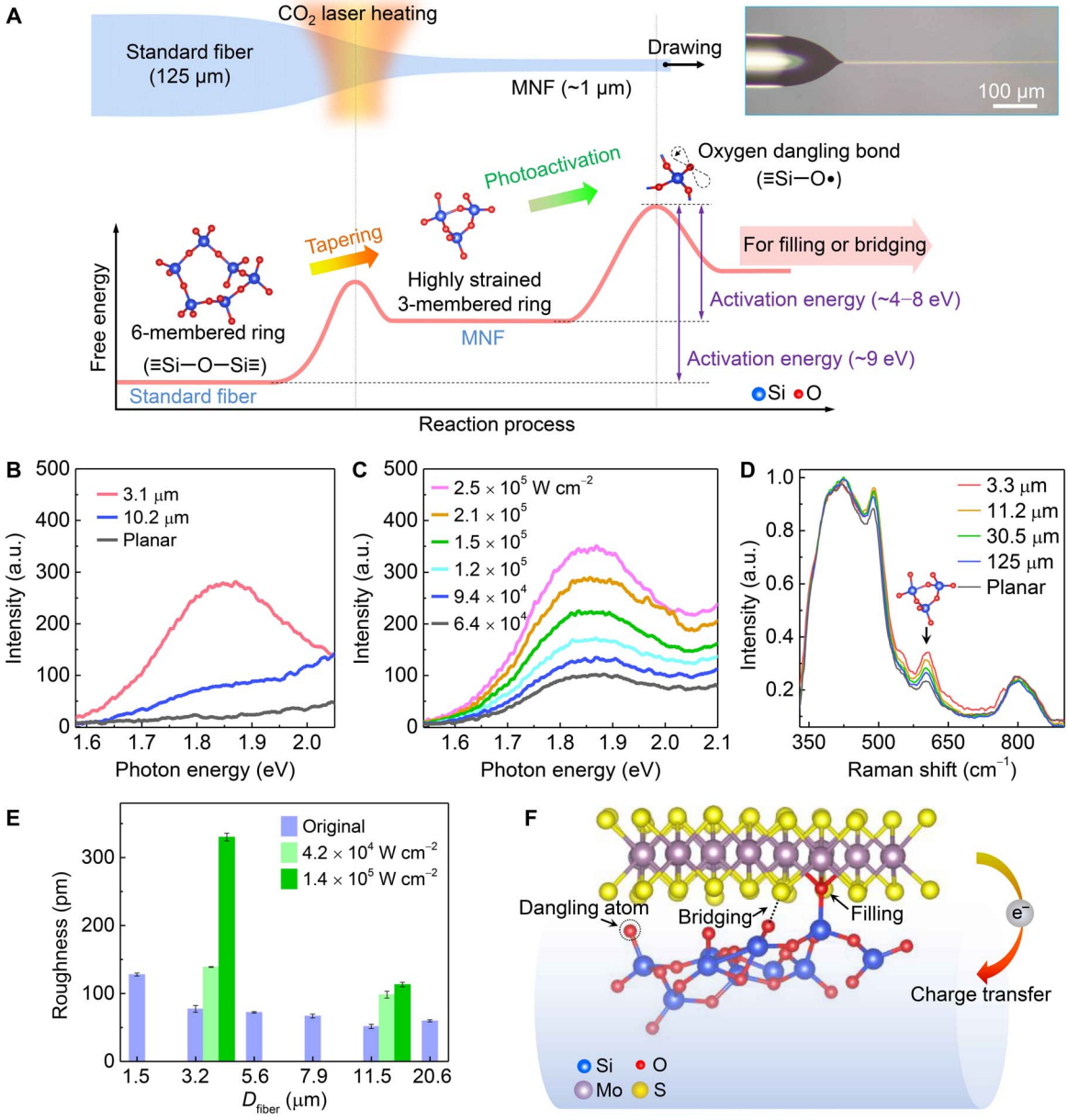

Fig. 1. Mechanism of photoactivation-induced PL enhancement. (**A**) Schematic illustration of generation of oxygen dangling bands from a tapered fiber. First, the CO_2 laser heating and drawing process breaks six-membered siloxane rings in a standard fiber (125 μm) into highly strained three-membered rings in a MNF (~1 μm), and then, the irradiation using a 532-nm CW laser activates the highly strained rings to generate oxygen dangling bonds (≡Si—O·). The tapering process greatly lowers the activation energy from ≡Si—O—Si≡ to ≡Si—O·. The generated oxygen dangling atoms are reactive and can fill or bride with outer atoms. Inset: Optical image of a MNF tapered from a standard fiber. (**B**) PL spectra from different microfibers and a planar substrate under excitation intensity of 2.1×10^5 W cm^{-2}. a.u., arbitrary units. (**C**) PL spectra of the microfiber (D_{fiber} = 3.1 μm) under different excitation intensity. (**D**) Raman spectra collected from different silica substrates. The intensity of the 606 cm^{-1} peak reflects the numbers of strained three-membered rings. (**E**) Surface roughness of different as-drawn original microfibers in the tapering (blue histogram) and high-intensity light irradiation (green histogram) process. (**F**) The generated oxygen dangling atoms can fill the sulfur vacancies, bridge with neighboring sulfur atoms, and form localized sites by transferring electrons from MoS_2, leading to enhanced PL emission.

These spectral red shifts arise from the biaxial tensile strain induced by the mismatch of thermal expansion coefficients between MoS_2 and silica (*29*). High-resolution AFM scans (section S9) and density functional theory calculations (section S10) also reveal that the tensile strain is less than 0.5%, which is within the expected range for CVD-grown monolayer MoS_2 (*17*). These results also reflect that the tensile strain increases as the MNF diameter decreases; however, it is known that strain is not conducive to the PL emission of monolayer MoS_2 grown on silica substrates. So next we discuss the causes of PL enhancement of monolayer MoS_2 on MNFs, we no longer consider the strain factor.

We use the 532-nm CW laser to activate the monolayer MoS_2/MNF structures that are suspended in air (see Materials and Methods and section S2). Figure 3A shows time-dependent integrated PL intensity

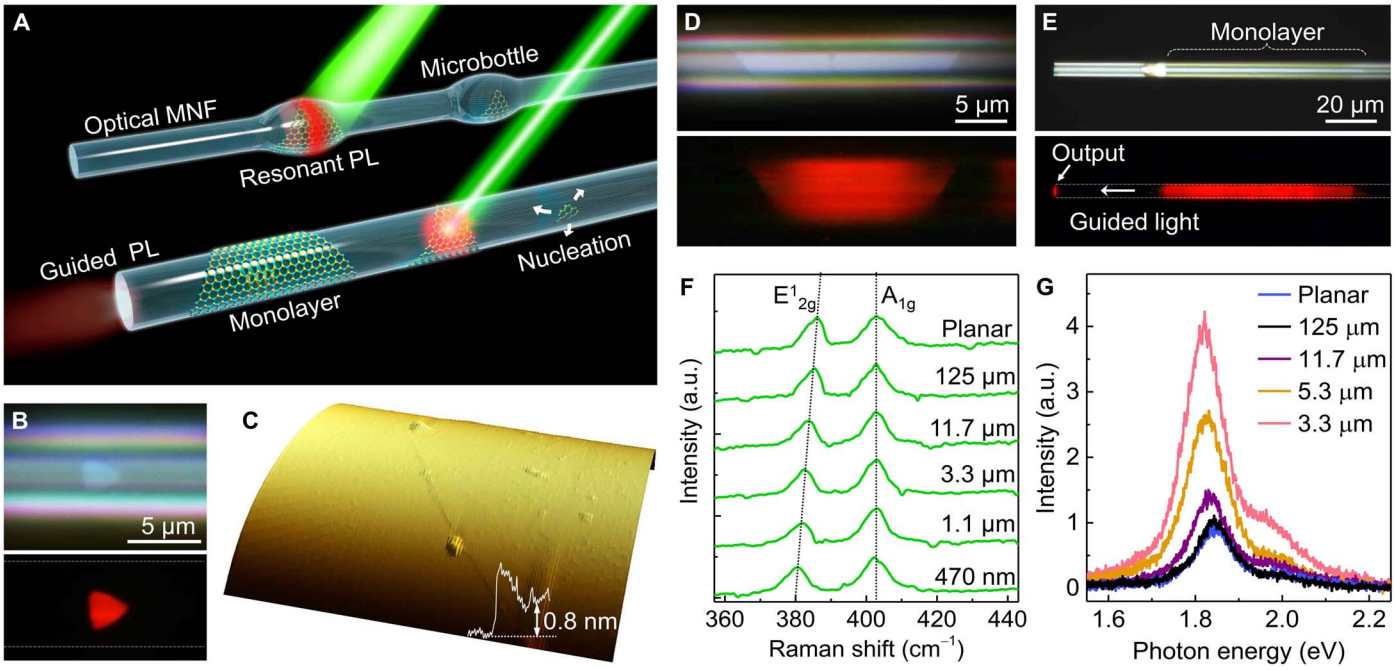

Fig. 2. Monolayer MoS_2 grown on MNFs. (**A**) Conceptual illustration of monolayer MoS_2 grown on MNFs with uniform diameters and with microbottle structures. A single-crystal triangular domain first nucleates on the MNF surface and then laterally grows into a large-area monolayer structure. A 532-nm CW laser is used to excite the PL emissions, some of which can be guided along the MNF or resonate in the MNF and microbottle structures. (**B**) Optical and PL images of a triangular layered MoS_2 on a microfiber (D_{fiber} = 6.1 μm), with (**C**) a thickness of ~0.8 nm confirmed by an AFM scan. (**D**) Optical and PL images showing clean surface and two sharp boundary edge of a MoS_2 monolayer/microfiber structure (D_{fiber} = 5.5 μm). (**E**) Optical and PL images showing a large-area monolayer/microfiber (D_{fiber} = 5.4 μm). Some guided emission is emitted at the distal end of the microfiber. (**F**) Raman spectra and (**G**) PL spectra of monolayer MoS_2 grown on different substrates. Both the strain-sensitive E^1_{2g} mode and PL spectral peaks exhibit red shifts as the MNF diameters decrease.

of a small triangular monolayer MoS_2 on a microfiber (D_{fiber} = 3.3 μm) under activation intensity of 2×10^5 W cm^{-2}. We can see that the generated PL intensity is gradually increased by 43 times before its saturation, compared to the initial intensity value upon the light irradiation. Figure 3B records its PL spectra evolution with time. On the basis of the results obtained under low temperatures and different atmospheric pressures, as well as the time-resolved PL measurement, the spectra can be deconvoluted into three peaks, neutral exciton (A^0, 1.85 eV), negatively charged trion (A^-, 1.81 eV), and defect-related localized exciton (A^D, 1.75 eV) emissions (section S11). We find that the A^0 peak grows rapidly and eventually becomes dominant. In contrast, the PL intensity of the monolayers grown either on a planar silica substrate or on a standard fiber remains constant throughout, while the PL intensity of a monolayer/microfiber with D_{fiber} = 11.7 μm is increased but by only 2.5 times. We also noticed that the initial tapering process can directly generate some oxygen dangling bonds by mechanically breaking the siloxane bonds, which can explain the higher original PL intensity of monolayers on thinner MNFs before photoactivation, as shown in Figs. 2G and 3A. After photoactivation, the steady-state PL spectra of the MoS_2 monolayer/microfiber (Fig. 3C) are always dominated by the A^0 peaks (~1.85 eV) as pump intensity (I_{pump}) increases from 10^{-1} to 10^4 W cm^{-2} (Fig. 3D), in contrast to the large red-shift phenomenon in the nonactivated samples (section S12).

In addition, no whispering-gallery mode (WGM) oscillation is observed in the PL spectra, and the PL enhancement is unaffected when the monolayer/MNFs are placed on a lossy substrate (section S13), which indicates that the cavity-enhanced emission can be ignored here (*30*). Nevertheless, when removed from the MNFs, the monolayers exhibit reduced PL intensity and no PL enhancement either before or after irradiation (section S14). These results shown above confirm that the oxygen dangling bonds generated by photoactivation lead to the PL enhancement. Because of the reduced activation energy from siloxane bonds to free oxygen dangling bonds by the taper-drawing process, the photoactivation process can be easily achieved using a CW laser with an activation threshold of ~5×10^4 W cm^{-2} (section S15). Furthermore, we also observe the photoactivation-induced PL enhancement of MoS_2 monolayers in other silica substrates such as microbottles as shown in Fig. 2A (section S7). We also observe similar PL enhancements of about 15 times in photoactivated monolayer $MoSe_2$ grown on a microfiber (section S16), which strongly suggests that our strategy is applicable to both sulfur- and selenide-based monolayer TMDs.

Using a calibrated rhodamine 6G film (section S17), we extract the PL QYs of as-photoactivated MoS_2 monolayer (D_{fiber} = 3.3 μm) as pump intensity increases from 10^{-1} to 10^4 W cm^{-2} (Fig. 3D, red data). For comparison under the same experimental conditions, we take nontransferred CVD-grown planar monolayer MoS_2 as the reference. Compared with the planar sample with a QY of <0.05%, the QY of the photoactivated sample is strongly enhanced by more than two orders of magnitude in a wide pump dynamic range. At low I_{pump} (<1 W cm^{-2}), the QY of our sample reaches ~30% and is comparable to that of the CVD-grown MoS_2 monolayers by superacid treatment (*23*). Notably, as the I_{pump} increases from 10 to 10^3 W cm^{-2}, the QY of our sample exhibits 6 to 20 times higher than those by superacid treatment (*23*), and the QY remains >1% even as the I_{pump}

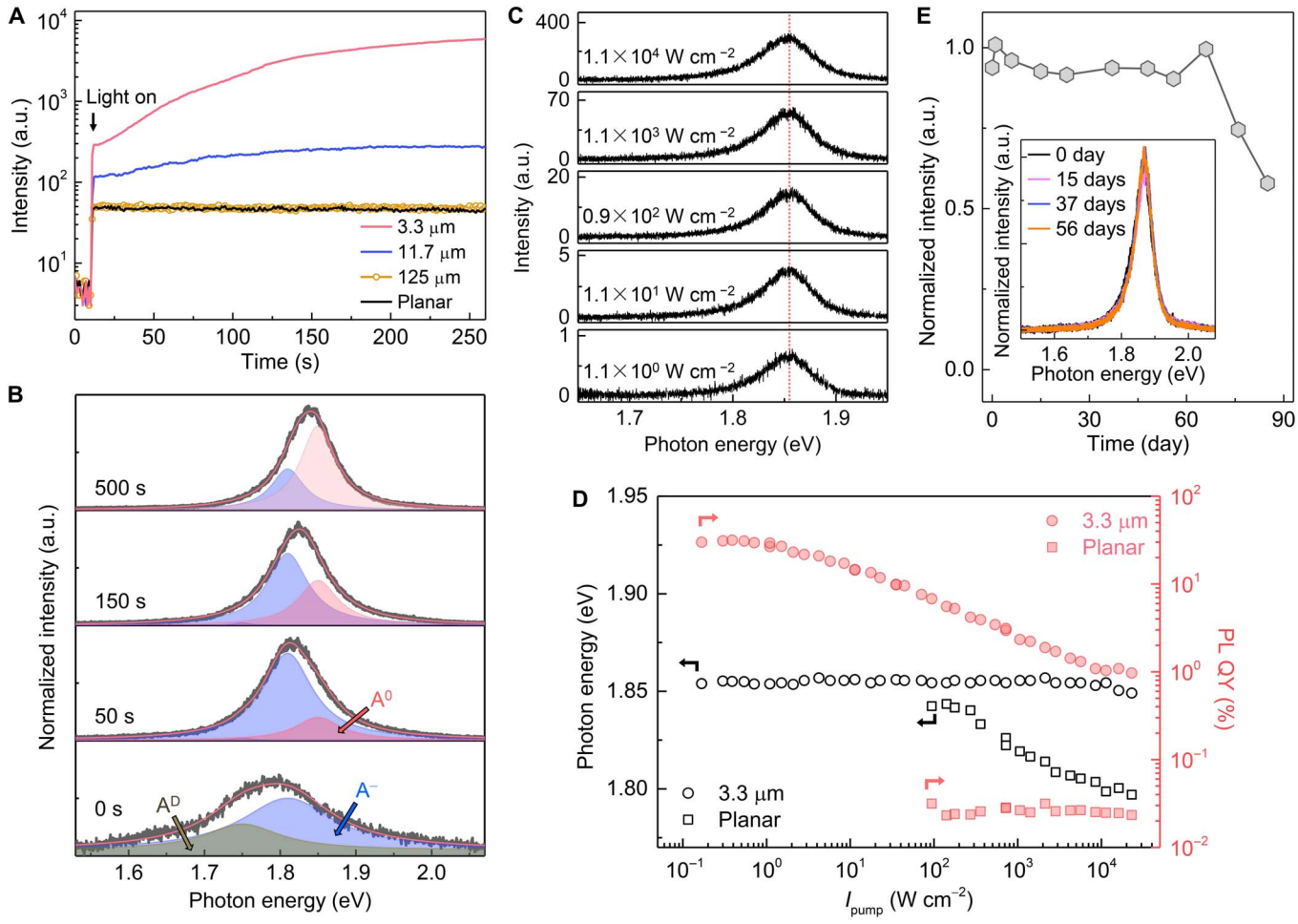

Fig. 3. Photoactivation-enhanced PL QYs. (**A**) Time-dependent PL intensity of MoS_2 monolayers grown on different substrates, under activation intensity of 2×10^5 W cm^{-2} using a 532-nm CW laser. (**B**) PL spectra of the monolayer/microfiber (D_{fiber} = 3.3 μm) at different irradiation time, which are deconvoluted into three emissions of A^0 at 1.85 eV, A^- at 1.81 eV, and A^D at 1.75 eV. (**C**) Steady-state PL spectra of the sample after photoactivation with increasing I_{pump} from 10^{-1} to 10^4 W cm^{-2}, all of which are dominant by the A^0 peaks (~1.85 eV). (**D**) Pump-dependent peak positions (black data) and PL QYs (red data) in the as-photoactivated monolayer MoS_2 (solid circles). A planar sample is also provided for reference (open squares). (**E**) Long-term stability of an as-photoactivated MoS_2 monolayer. Inset: Normalized PL spectra collected at different time.

approaches to 10^4 W cm^{-2}. In addition, our as-photoactivated samples are very stable under ambient conditions and can retain identical spectral features including intensity and emission profiles for several months (Fig. 3E, inset).

Since optical microfiber and microbottle structures themselves can serve as good optical microcavities (*31*–*33*), the high QY and stable PL emissions make as-photoactivated MoS_2 monolayers a good choice for direct generation of lasing at room temperature. We first use the 532-nm CW laser to excite an as-activated monolayer MoS_2/microfiber with D_{fiber} = 5.4 μm to realize a CW WGM lasing action, with the typical PL emission spectra dependent on I_{pump} shown in Fig. 4A. A sharp emission peak with a wavelength of 688.1 nm (corresponding to TM^1_{32} mode; see section S18) and a measured full width at half maximum (FWHM) of ~1.97 nm is observed, corresponding to a quality factor of 350. The measured lasing threshold is ~70 W cm^{-2} for a best fitted spontaneous emission factor (β) of 0.15 (section S19). Around this threshold value, we can estimate the QY of the activated monolayer MoS_2 to be ~7% by simply comparing with the I_{pump}-QY dependence in Fig. 3D. This QY value is similar to that of the monolayer WS_2 at 10 K (*8*), which is integrated in a WGM microdisk cavity with a quality factor of ~2600; however, the lasing threshold (5 to 8 MW cm^{-2}) in this case is five orders of magnitude higher than that in our work.

Owing to the better ability of the prolate microbottle structure to couple the spontaneous PL emissions into the resonant modes than that of the cylindrical microfiber structure (see schematic in Fig. 2A) (*31*, *32*), we further use an as-activated prolate monolayer MoS_2/microbottle (outer diameter, 5.5 μm) to realize a low-threshold CW lasing action. The I_{pump}-dependent PL emission spectra are shown in Fig. 4B. The threshold at a wavelength of 682.5 nm (TM^1_{31}; section S18) is reduced to approximately 5 W cm^{-2} (Fig. 4C) for a best fitted β of 0.5. This threshold value is two orders of magnitude lower than the room-temperature threshold obtained in monolayer MoS_2–based microsphere cavities (typically ~380 W cm^{-2}) (*11*) and is also comparable to that in a monolayer $MoTe_2$–based nanobeam cavity with a high quality factor of ~5603 (~6.6 W cm^{-2}) (*9*). With increasing I_{pump}, the FWHM shows an obvious narrowing to 0.58 nm (Fig. 4D), corresponding to a quality factor of 1177. For the threshold of

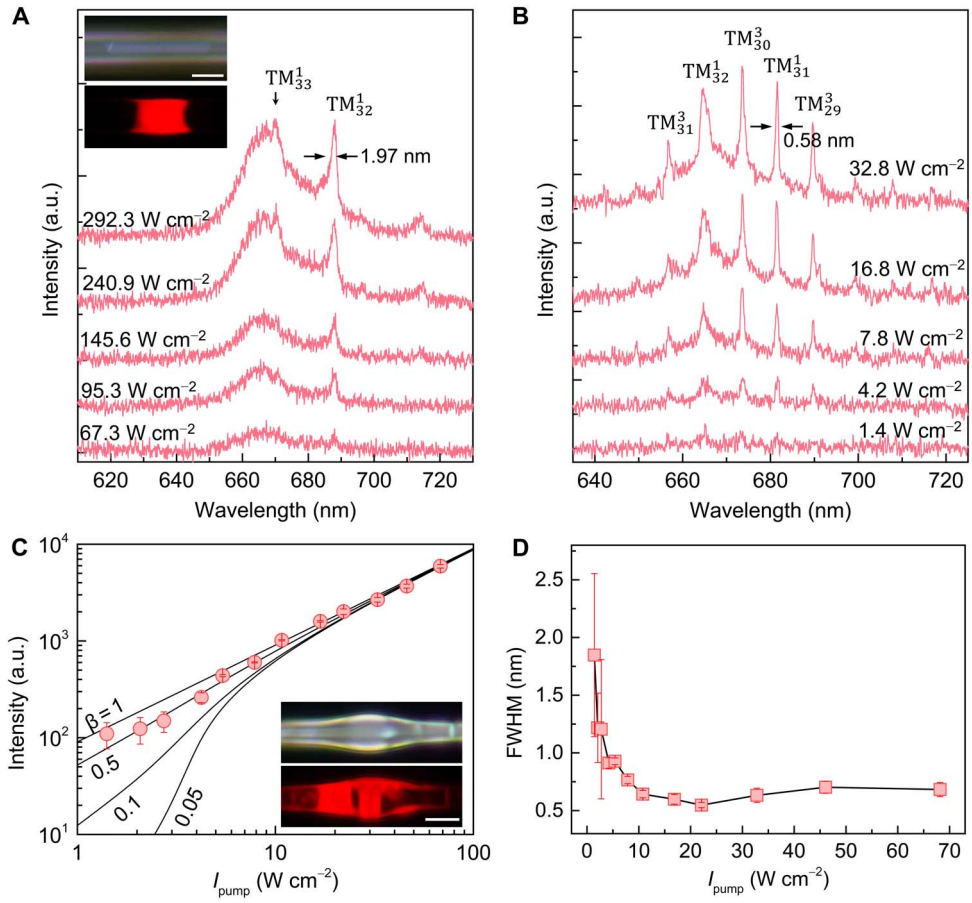

Fig. 4. Room-temperature CW lasing in as-photoactivated monolayer MoS_2. (**A**) Steady-state PL spectra in an as-photoactivated MoS_2 monolayer/microfiber (D_{fiber} = 5.4 μm) with increasing I_{pump} using the 532-nm CW laser, in which a strong 688.1-nm peak (TM^1_{31} mode) increases quickly from spontaneous emission to lasing. Inset: Optical and PL images of the monolayer/microfiber. Scale bar, 5 μm. (**B**) Steady-state PL spectra in an as-photoactivated MoS_2 monolayer/microbottle (outer diameter, 5.5 μm) with increasing I_{pump}, in which WGM oscillations are observed. (**C**) Light in–light out curve for a 682.5-nm lasing peak (TM^1_{31} mode) in the monolayer/microbottle on a log-log scale, in which a β of 0.5 is the best fit to the experimental data. Inset: Optical and PL images the monolayer/microbottle. Scale bar, 5 μm. (**D**) Pump-dependent FWHM of the 682.5-nm peak, which narrows quickly as I_{pump} exceeds the lasing threshold (5 W cm^{-2}).

~5 W cm^{-2}, the QY of the activated monolayer MoS_2 estimated from Fig. 3D is about 19%. Such a high QY can provide sufficient optical gain to generate room-temperature CW lasing with low threshold and without the need of high-quality factor optical microcavities. In addition, we also observe that the other four resonant modes of this monolayer MoS_2/microbottle exhibit the lasing performance (section S20). Similar lasing behavior is also observed in five other photoactivated samples on microfibers and microbottles (section S21), indicating the good repeatability of our approach.

DISCUSSION

Our work demonstrates substantially enhanced and stable room-temperature PL QYs of monolayer MoS_2 grown on silica MNFs in a wide pump dynamic range, using a simple photoactivation method. The taper-drawing process greatly lowers the photoactivation energy and allows fast completion of the entire photoactivation process in a few minutes with a CW laser. In addition, this noncontact photoactivation process does not require any sample transfer and manipulation, ensuring the high crystal quality of as-grown monolayers. These unique advantages enable us to directly realize low-threshold CW lasing without the use of high-quality factor optical microcavities. In addition, the direct growth of monolayer TMDs on MNF structures enables their seamless integration with standard optical fiber systems and also provides the opportunity to greatly enhance the interaction of light with monolayer TMDs using a waveguiding excitation approach (*33*). More generally, the underlying mechanism present here has been demonstrated as an efficient method to modulate the carrier density in monolayer TMDs and can also be applied to other two-dimensional semiconductor materials on silica substrates. We foresee that our photoactivation method for single-crystal TMD monolayer/MNF structures provides an exciting direction for various integrated applications ranging from low-threshold coherent light sources (*34*) and nonlinear optics (*35*) to optoelectronics (*36*).

MATERIALS AND METHODS

Fabrication of MNF and microbottle structures

MNF and microbottle structures used in this work were fabricated by a commonly used taper-drawing approach from standard communication fiber (SMF-28, Corning) (*21*, *22*, *37*). As shown in section S1, a bare fiber with a length of ~3 cm was suspended and fixed on two

motor-driven stages. A CO_2 laser (Ti60W-HS, Synrad Inc.) connected with a signal generator was used as a heating source. Its laser beam with a diameter of 2.5 mm was first expanded to a beam with a diameter of 8 mm by a pair of ZnSe lenses and then focused onto the bare fiber with a focus area of ~50 μm. The output power of the CO_2 laser was controlled by adjusting the duty circle of the electronic pulse from the signal generator. Thus, we obtained a desirable heating temperature for the fabrication. A microscope equipped with a 20× objective and a charge-coupled device (CCD) camera was used for monitoring the fabrication process. By controlling the drawing speed and the heating temperature, MNFs with different diameters ranging from ~300 nm to tens of micrometers can be obtained.

Microbottle structures were obtained by further processing the as-fabricated MNFs. An MNF was first moved away from the laser focus for a certain distance. Then, the two fixed points were slightly moved toward each other to squeeze the fiber inversely. At the same time, we increased the laser power. Because of surface tension, the heated MNF will readily form a prolate shape structure, which was usually called microbottle (*31*, *32*). The outer diameters of as-fabricated microbottles were determined by the diameters of the MNFs used and the squeezing time during the heating process.

Optical measurements of Raman, PL, and lasing spectra

The experimental setup is shown in section S2. We used a CW 532-nm laser with a narrow spectral linewidth of <0.01 pm as the excitation light source (MSL-FN-532, Changchun New Industries Optoelectronics Technology Co. Ltd.). The laser was linear polarized with a fundamental transverse electromagnetic mode (TEM_{00}), and the polarization of the laser beam irradiated on the samples was parallel to the axis of the MNFs. The laser beam with a diameter of 1.5 mm was reflected by a pair of silver mirrors to ensure horizontal propagation. A neutral density filter was used to control the incident optical power with intensity ranging from 0 to 10^7 W cm^{-2}. Two optical lenses, with focal lengths of 10 mm, were used to adjust the diameters of the beam. By changing the distance between the two lenses, we obtained different sizes of the focused spots on the monolayer TMD samples through a 100× objective (LU Plan, Nikon), with diameters ranging from ~1 to ~100 μm. The monolayer samples on MNFs and microbottles used in this work were protruded from a glass substrate edge, i.e., the samples were suspended in air during the optical measurements. In experiments, the focused light spots with different diameters were used. For instance, in the analysis of Raman emissions (Figs. 1B and 2F), PL emissions (Fig. 2G), photoactivation process, and PL QYs (Fig. 3), the excitation spots have a diameter of ~1 μm. But for lasing generation in Fig. 4, to obtain sufficient optical gain, we used the excitation spots with large diameters to cover the whole monolayer samples. The light emissions from monolayer samples on different substrates were collected using the same 100× objective, directed through a dichroic filter (NFD01-532-25x36, Semrock) and a 532-nm notch filter (NF01-532 U-25, Semrock), and then split by a beam splitter to a spectrometer (iHR550, HORIBA) for spectral analysis and to a CCD camera (DS-Ri1, Nikon) for imaging.

Synthesis of TMD monolayers

We used a CVD method to grow TMD monolayers in a horizontal quartz tube mounted inside a single-zone furnace (*23*, *38*). As shown in section S4, an alumina boat with 200 mg of sulfur powder (≥99.5%; Aladdin Inc.) was first placed upstream to the edge of the furnace, and an alumina boat with 20 mg of molybdenum (VI) oxide (MoO_3) powder (≥99%; Sinopharm Chemical Reagent Co. Ltd.) was placed at the center of the heating zone. To grow monolayer MoS_2 on the MNFs, several as-drawn MNFs were placed on an inverted boat next to the MoO_3 boat downstream. The tips of the MNFs protrude from the top of the inverted boat with a distance of ~2 mm. A thick silica substrate (dimensions of 3 cm by 3 cm by 5 mm) was placed on the MNFs to prevent them from being blown off by the airflow. To fabricate monolayer MoS_2 on the planar substrates, several planar silica substrates (dimensions of 1 cm by 5 cm by 1 mm) were placed above the MoO_3 boat. Before heating, high-purity argon gas was introduced into the quartz tube at a flow rate of 200 standard cubic centimeters per minute (sccm) to purge air from the tube. After 20 min, the furnace was rapidly heated to 850°C at a rate of 20°C min^{-1}, while atmospheric pressure was maintained. After 4 min of growth at 850°C, the temperature was reduced to room temperature naturally.

To grow $MoSe_2$ monolayers, an alumina boat with 100 mg of selenium powder (≥99.5%, Aladdin Inc.) was placed upstream to the edge of the furnace, and an alumina boat with 2 mg of MoO_3 powder was placed at the center of the heating zone. High-purity argon gas was introduced into the quartz tube at a flow rate of 80 sccm. The grown temperature was 820°C and the grown time was 5 min.

SUPPLEMENTARY MATERIALS

Supplementary material for this article is available at http://advances.sciencemag.org/cgi/content/full/5/11/eaax7398/DC1

Supplementary Text
Section S1. Fabrication of MNF and microbottle structures
Section S2. Experimental setup for Raman, PL, and lasing spectra measurements
Section S3. Oxygen dangling bonds and charge transfer
Section S4. Synthesis of TMD monolayers
Section S5. Single-crystal nature
Section S6. Monolayer MoS_2 grown on nanofibers
Section S7. PL enhancement on a microbottle structure
Section S8. Absorption spectra
Section S9. High-resolution AFM scan
Section S10. Calculation of the band structure
Section S11. Determination of neutral excitons, trions, and defect-related localized excitons
Section S12. Spectral changes in monolayer MoS_2 without photoactivation
Section S13. Investigation of cavity effect in the PL enhancement
Section S14. Optical properties in monolayer MoS_2 removed from MNFs
Section S15. Photoactivation threshold
Section S16. PL enhancement in monolayer $MoSe_2$ grown on MNFs
Section S17. Calibration of PL QYs
Section S18. Simulation of lasing cavity modes
Section S19. Rate equation analysis
Section S20. Lasing performance in other resonant modes
Section S21. Reproducibility of our approach
Fig. S1. Fabrication of MNF and microbottle structures.
Fig. S2. Experimental setup for Raman, PL, and lasing measurements.
Fig. S3. Numerical simulation of oxygen dangling bonds and charge transfer.
Fig. S4. Experimental setup for growing monolayer MoS_2 using a CVD method.
Fig. S5. Single-crystal nature.
Fig. S6. Monolayer MoS_2 grown on an optical nanofiber.
Fig. S7. PL enhancement on a microbottle structure.
Fig. S8. Absorption spectra of monolayer MoS_2 on a planar silica substrate and different fibers.
Fig. S9. High-resolution AFM scan.
Fig. S10. DFT calculations of the band structure of monolayer MoS_2.
Fig. S11. Spectral responses obtained under low temperatures and different atmospheric pressures, and time-resolved PL measurement.
Fig. S12. Spectral changes in monolayer MoS_2 without photoactivation.
Fig. S13. Investigation of cavity effect in the PL enhancement.
Fig. S14. Optical properties in monolayer MoS_2 removed from MNFs.
Fig. S15. Pump intensity dependent PL intensity of monolayer MoS_2 on different substrates.
Fig. S16. PL enhancement in monolayer $MoSe_2$ grown on MNFs.
Fig. S17. Simulation of lasing cavity modes.

Fig. S18. Rate equation analysis.
Fig. S19. Lasing performance in other resonant modes.
Fig. S20. Typical lasing spectra and light in–light out curves of the lasing performance in typical five different samples.
Table S1. Details of electron transfer in the structure of fig. S3.
Table S2. Summary of the accuracy in QY measured in typical five samples.
Table S3. Comparison of the fitting parameters of microfiber and microbottle of rate equation analysis.
Table S4. Summary of the lasing thresholds of samples shown in fig. S20.
References (*39*, *40*)

REFERENCES AND NOTES

1. F. Xia, H. Wang, D. Xiao, M. Dubey, A. Ramasubramaniam, Two-dimensional material nanophotonics. *Nat. Photonics* **8**, 899–907 (2014).
2. J. Shang, C. Cong, L. Wu, W. Huang, T. Yu, Light sources and photodetectors enabled by 2D semiconductors. *Small Methods* **2**, 1800019 (2018).
3. W. Zheng, Y. Jiang, X. Hu, H. Li, Z. Zeng, X. Wang, A. Pan, Light emission properties of 2D transition metal dichalcogenides: Fundamentals and applications. *Adv. Opt. Mater.* **6**, 1800420 (2018).
4. L. Yuan, L. B. Huang, Exciton dynamics and annihilation in WS_2 2D semiconductors. *Nanoscale* **7**, 7402–7408 (2015).
5. M. Amani, D.-H. Lien, D. Kiriya, J. Xiao, A. Azcatl, J. Noh, S. R. Madhvapathy, R. Addou, K. C. Santosh, M. Dubey, K. Cho, R. M. Wallace, S.-C. Lee, J.-H. He, J. W. Ager III, X. Zhang, E. Yablonovitch, A. Javey, Near-unity photoluminescence quantum yield in MoS_2. *Science* **350**, 1065–1068 (2015).
6. H. Kim, G. Ahn, J. Cho, M. Amani, J. Mastandrea, C. Groschner, D. Lien, Y. Zhao, J. Ager, M. Scott, D. Chrzan, A. Javey, Synthetic WSe_2 monolayers with high photoluminescence quantum yield. *Sci. Adv.* **5**, eaau4728 (2019).
7. S. Wu, S. Buckley, J. R. Schaibley, L. Feng, J. Yan, D. G. Mandrus, F. Hatami, W. Yao, J. Vuckovic, A. Majumdar, X. Xu, Monolayer semiconductor nanocavity lasers with ultralow thresholds. *Nature* **520**, 69–72 (2015).
8. Y. Ye, Z. J. Wong, X. Lu, X. Ni, H. Zhu, X. Chen, Y. Wang, X. Zhang, Monolayer excitonic laser. *Nat. Photonics* **9**, 733–737 (2015).
9. Y. Li, J. Zhang, D. Huang, H. Sun, F. Fan, J. Feng, Z. Wang, C. Z. Ning, Room-temperature continuous-wave lasing from monolayer molybdenum ditelluride integrated with a silicon nanobeam cavity. *Nat. Nanotechnol.* **12**, 987–992 (2017).
10. J. Shang, C. Cong, Z. Wang, N. Peimyoo, L. Wu, C. Zou, Y. Chen, X. Y. Chin, J. Wang, C. Soci, W. Huang, T. Yu, Room-temperature 2D semiconductor activated vertical-cavity surface-emitting lasers. *Nat. Commun.* **8**, 543 (2017).
11. L. Zhao, Q. Shang, Y. Gao, J. Shi, Z. Liu, J. Chen, Y. Mi, P. Yang, Z. Zhang, W. Du, M. Hong, Y. Liang, J. Xie, X. Hu, B. Peng, J. Leng, X. Liu, Y. Zhao, Y. Zhang, Q. Zhang, High-temperature continuous-wave pumped lasing from large-area monolayer semiconductors grown by chemical vapor deposition. *ACS Nano* **12**, 9390–9396 (2018).
12. J. Kang, D. Shin, S. Bae, B. H. Hong, Graphene transfer: Key for applications. *Nanoscale* **4**, 5527–5537 (2012).
13. S. Tongay, J. Zhou, C. Ataca, J. Liu, J. S. Kang, T. S. Matthews, L. You, J. Li, J. C. Grossman, J. Wu, Broad-range modulation of light emission in two-dimensional semiconductors by molecular physisorption gating. *Nano Lett.* **13**, 2831–2836 (2013).
14. S. Mouri, Y. Miyauchi, K. Matsuda, Tunable photoluminescence of monolayer MoS_2 via chemical doping. *Nano Lett.* **13**, 5944–5948 (2013).
15. S. Tongay, J. Suh, C. Ataca, W. Fan, A. Luce, J. S. Kang, J. Liu, C. Ko, R. Raghunathanan, J. Zhou, F. Ogletree, J. Li, J. C. Grossman, J. Wu, Defects activated photoluminescence in two-dimensional semiconductors: Interplay between bound, charged, and free excitons. *Sci. Rep.* **3**, 2657 (2013).
16. Y. Lee, G. Ghimire, S. Roy, Y. Kim, C. Seo, A. K. Sood, J. I. Jang, J. Kim, Impeding exciton-exciton annihilation in monolayer WS_2 by laser irradiation. *ACS Photonics* **5**, 2904–2911 (2018).
17. R. Roldan, A. Castellanos-Gomez, E. Cappelluti, F. Guinea, Strain engineering in semiconducting two-dimensional crystals. *J. Phys. Condens. Matter* **27**, 313201 (2015).
18. M. Amani, P. Taheri, R. Addou, G. H. Ahn, D. Kiriya, D.-H. Lien, J. W. Ager III, R. M. Wallace, A. Javey, Recombination kinetics and effects of superacid treatment in sulfur- and selenium-based transition metal dichalcogenides. *Nano Lett.* **16**, 2786–2791 (2016).
19. R. A. McKee, F. J. Walker, M. F. Chisholm, Physical structure and inversion charge at a semiconductor interface with a crystalline oxide. *Science* **293**, 468–471 (2001).
20. K. Dolui, I. Rungger, S. Sanvito, Origin of the *n*-type and *p*-type conductivity of MoS_2 monolayers on a SiO_2 substrate. *Phys. Rev. B* **87**, 165402 (2013).
21. R. Ismaeel, T. Lee, M. Ding, M. Belal, G. Brambilla, Optical microfiber passive components. *Laser Photonics Rev.* **7**, 350–384 (2013).
22. X. Guo, Y. Ying, L. Tong, Photonic nanowires: From subwavelength waveguides to optical sensors. *Acc. Chem. Res.* **47**, 656–666 (2014).
23. M. Amani, R. A. Burke, X. Ji, P. Zhao, D.-H. Lien, P. Taheri, G. H. Ahn, D. Kirya, J. W. Ager III, E. Yablonovitch, J. Kong, M. Dubey, A. Javey, High luminescence efficiency in MoS_2 grown by chemical vapor deposition. *ACS Nano* **10**, 6535–6541 (2016).
24. K. Awazu, H. Kawazoe, Strained Si-O-Si bonds in amorphous SiO_2 materials: A family member of active centers in radio, photo, and chemical responses. *J. Appl. Phys.* **94**, 6243–6262 (2003).
25. L. Skuja, M. Hirano, H. Hosono, K. Kajihara, Defects in oxide glasses. *Phys. Status Solidi C* **2**, 15–24 (2005).
26. K. B. Wiberg, The concept of strain in organic chemistry. *Angew. Chem. Int. Ed. Engl.* **25**, 312–322 (1986).
27. H. Nan, Z. Wang, W. Wang, Z. Liang, Y. Lu, Q. Chen, D. He, P. Tan, F. Miao, X. Wang, J. Wang, Z. Ni, Strong photoluminescence enhancement of MoS_2 through defect engineering and oxygen bonding. *ACS Nano* **8**, 5738–5745 (2014).
28. H. J. Conley, B. Wang, J. I. Ziegler, R. F. Haglund Jr., S. T. Pantelides, K. I. Bolotin, Bandgap engineering of strained monolayer and bilayer MoS_2. *Nano Lett.* **13**, 3626–3630 (2013).
29. Z. Liu, M. Amani, S. Najmaei, Q. Xu, X. Zou, W. Zhou, T. Yu, C. Qiu, A. G. Birdwell, F. J. Crowne, R. Vajtai, B. I. Yakobson, Z. Xia, M. Dubey, P. M. Ajayan, J. Lou, Strain and structure heterogeneity in MoS_2 atomic layers grown by chemical vapour deposition. *Nat. Commun.* **5**, 5246 (2014).
30. A. Krasnok, S. Lepeshov, A. Alu, Nanophotonics with 2D transition metal dichalcogenides Invited. *Opt. Express* **26**, 15972–15994 (2018).
31. M. Sumetsky, Whispering-gallery-bottle microcavities: The three-dimensional etalon. *Opt. Lett.* **29**, 8–10 (2004).
32. F. Gu, F. Xie, X. Lin, S. Linghu, W. Fang, H. Zeng, L. Tong, S. Zhuang, Single whispering-gallery-mode lasing in polymer bottle microresonators via spatial pump engineering. *Light Sci. Appl.* **6**, e17061 (2017).
33. F. Gu, H. Yu, P. Wang, Z. Yang, L. Tong, Light-emitting polymer single nanofibers via waveguiding excitation. *ACS Nano* **4**, 5332–5338 (2010).
34. R.-M. Ma, R. F. Oulton, Applications of nanolasers. *Nat. Nanotechnol.* **14**, 12–22 (2019).
35. M. Liu, X. Yin, E. Ulin-Avila, B. Geng, T. Zentgraf, L. Ju, F. Wang, X. Zhang, A graphene-based broadband optical modulator. *Nature* **474**, 64–67 (2011).
36. Z. Jin, F. Ye, X. Zhang, S. Jia, L. Dong, S. Lei, R. Vajtai, J. T. Robinson, J. Lou, P. M. Ajayan, Near-field coupled integrable two-dimensional InSe photosensor on optical fiber. *ACS Nano* **12**, 12571–12577 (2018).
37. F. Gu, L. Zhang, Y. Zhu, H. Zeng, Free-space coupling of nanoantennas and whispering-gallery microcavities with narrowed linewidth and enhanced sensitivity. *Laser Photonics Rev.* **9**, 682–688 (2015).
38. F. Gu, Z. Yang, H. Yu, J. Xu, P. Wang, L. Tong, A. Pan, Spatial bandgap engineering along single alloy nanowires. *J. Am. Chem. Soc.* **133**, 2037–2039 (2011).
39. H. Shi, H. Pan, Y.-W. Zhang, B. I. Yakobson, Quasiparticle band structures and optical properties of strained monolayer MoS_2 and WS_2. *Phys. Rev. B* **87**, 155304 (2013).
40. H. Zhang, Y. Ma, Y. Wan, X. Rong, Z. Xie, W. Wang, L. Dai, Measuring the refractive index of highly crystalline monolayer MoS_2 with high confidence. *Sci. Rep.* **5**, 8440 (2015).

Acknowledgments: We thank H. Yu in South China University of Technology, G. Wang in University of Cambridge, and L. Tong and X. Lin in Zhejiang University for helpful suggestions. **Funding:** This work is supported by the National Natural Science Foundation of China (11604210 and 11674230) and the Shanghai Rising-Star Program (18QA1403200). **Author contributions:** F.G. conceived the idea and designed the research. F.L. and J.Y. performed the experiments, collected and analyzed the data, and wrote the paper. Z.G. performed the theoretical calculations and analysis and wrote the paper. S.L. and J.P. contributed in AFM analysis and time-resolved PL experiments. Z.Y., T.H., W.F., S.Z., and M.G. helped in data analysis and manuscript writing. All authors discussed the results and commented on the manuscript. **Competing interests:** The authors declare that they have no competing interests. **Data and materials availability:** All data needed to evaluate the conclusions in the paper are present in the paper and/or the Supplementary Materials. Additional data related to this paper may be requested from the authors.

Submitted 18 April 2019
Accepted 4 October 2019
Published 22 November 2019
10.1126/sciadv.aax7398

Citation: F. Liao, J. Yu, Z. Gu, Z. Yang, T. Hasan, S. Linghu, J. Peng, W. Fang, S. Zhuang, M. Gu, F. Gu, Enhancing monolayer photoluminescence on optical micro/nanofibers for low-threshold lasing. *Sci. Adv.* **5**, eaax7398 (2019).